2023 IEEE/RSJ International Conference on Intelligent Robots and Systems (IROS)
October 1-5, 2023. Detroit, USA

A New 1-mg Fast Unimorph SMA-Based Actuator for Microrobotics

Conor K. Trygstad, Xuan-Truc Nguyen, and Néstor O. Pérez-Arancibia

***Abstract*— We present a new unimorph actuator for microrobotics, which is driven by thin *shape-memory alloy* (SMA) wires. Using a passive-capillary-alignment technique and existing SMA-microsystem fabrication methods, we developed an actuator that is 7 mm long, has a volume of $0.45\,\text{mm}^3$, weighs 0.96 mg, and can achieve operation frequencies of up to 40 Hz as well as lift 155 times its own weight. To demonstrate the capabilities of the proposed actuator, we created an 8-mg crawler, the MiniBug, and a bioinspired 56-mg controllable water-surface-tension crawler, the WaterStrider. The MiniBug is 8.5 mm long, can locomote at speeds as high as 0.76 BL/s (*body-lengths per second*), and is the lightest fully-functional crawling microrobot of its type ever created. The WaterStrider is 22 mm long, and can locomote at speeds of up to 0.28 BL/s as well as execute turning maneuvers at angular rates on the order of 0.144 rad/s. The WaterStrider is the lightest controllable SMA-driven water-surface-tension crawler developed to date.**

I. Introduction

We envision the creation of autonomous millimeter-scale robots that can work together in swarms to execute tasks such as artificial pollination, insect-plague control, agricultural surveying, search and rescue, environmental monitoring, microfabrication, and robotic-assisted surgeries. In order for millimeter-scale robots to complete complex assignments and function autonomously, they must efficiently generate large forces relative to their size and weight. The most common actuators used in microrobotics are based on piezoelectric [1]–[4], electromagnetic [5]–[10], or *shape-memory alloy* (SMA) [11]–[15] technologies. Because of their wider frequency bandwidths, piezoelectric and electromagnetic microactuators are generally preferred over SMA-based systems. However, compared to SMA-based methods, these two actuation technologies exhibit significantly lower work densities and, additionally, electromagnetic microactuators have been shown to be difficult to operate outside laboratory settings. In [13], we introduced a 6-mg fast SMA-based microactuator; here, we present an actuator of the same type which is significantly lighter, smaller, and stronger for its size. In fact, this is the lightest and fastest SMA-based actuator reported to date; it weighs only 0.96 mg, has a length of 7 mm, has a volume of $0.45\,\text{mm}^3$, can produce functional displacements at frequencies of up to 40 Hz, and can lift 155 times its own weight. This achieved performance is a consequence of the actuator's mechanical design and structure, which is essentially composed of two parallel nitinol (56 % Nickel & 44 % Titanium) SMA wires with a diameter of 25.4 µm and a leaf spring used to facilitate the transition between the *twinned* and *detwinned martensite* phases of the SMA material during an actuation cycle [13]. This configuration is the key element that enables the actuator to operate at high frequencies (up to 40 Hz).

Fig. 1. **Two microrobots driven by the proposed SMA-based actuator.** The WaterStrider (left) is a 56-mg controllable robot with a body length of 22 mm that crawls on water by taking advantage of surface-tension phenomena. The MiniBug (right) is an 8-mg microrobot with a body length of 8.5 mm that crawls on land. This robot is the lightest fully-functional SMA-driven terrestrial crawler developed to date.

To test and demonstrate the capabilities of the proposed microactuator, we developed an 8-mg terrestrial crawler, the MiniBug, and a bioinspired 56-mg water-surface-tension crawler, the WaterStrider; these two robots are shown in Fig. 1. Inspired by the design introduced in [13], the MiniBug is the lightest fully-functional SMA-driven crawler ever created and represents significant progress toward miniaturization with respect to the crawling platforms in [13] and [14]. Specifically, the MiniBug has a length of 8.5 mm and can locomote at speeds of up to 0.76 BL/s (*body-lengths per second*). We envision that robots of this type can be equipped with micromanipulators and be used in swarms to execute tasks in structured environments with smooth surfaces; for example, to provide assistance in small-scale production lines. Inspired by the locomotion modes of common water-strider insects (*Gerris lacustris*), the WaterStrider prototype (see Fig. 1) has a lightweight structure and elliptical supporting feet with relatively large surface areas, which ensure that the generated surface-tension forces are strong enough to compensate gravity and allow the robot to stably stand on water. The two fin-like propulsors of this platform are independently driven by two of the proposed high-work-density actuators through four-bar transmissions designed and fabricated using the *smart composite microstructure* (SCM) method. During operation, the typical resulting stroke angles are on the order of 30 ° and directional control of the robot is achieved by changing their amplitudes in real time (see Section IV). In this case, through simple experiments and heuristic considerations, we

This work was partially funded by the Washington State University (WSU) Foundation and the Palouse Club through a Cougar Cage Award to N. O. Pérez-Arancibia. Additional funding was provided by the WSU Voiland College of Engineering and Architecture through a start-up fund to N. O. Pérez-Arancibia.

C. K. Trygstad and N. O. Pérez-Arancibia are with the School of Mechanical and Materials Engineering, Washington State University (WSU), Pullman, WA 99164-2920, USA (e-mail: conor.trygstad@wsu.edu (C. K. T.)); n.perezarancibia@wsu.edu (N. O. P.-A.)).

X.-T. Nguyen is with Flyby Robotics, Los Angeles, CA 90028, USA (e-mail: xuan-truc@flybydev.com).

2023 IEEE/RSJ International Conference on Intelligent Robots and Systems (IROS) | 978-1-6654-9190-7/23/$31.00 ©2023 IEEE | DOI: 10.1109/IROS55552.2023.10342518

aimed to maximize the hydrodynamic force output by taking advantage of fluid-structure-interaction phenomena, a matter of current and further research. The WaterStrider prototype in Fig. 1 can locomote at speeds of up to 0.28 BL/s and complete open-loop turning maneuvers at angular rates of up to 0.144 rad/s. We anticipate that in the near future, water-surface-tension crawlers of the WaterStrider type will be employed for geographical surveying and continuous water quality monitoring in lakes, dams, and rivers; for example, to quickly detect toxic spills or changes in hydrology.

The rest of the paper is organized as follows. Section II describes the design and fabrication of the proposed unimorph SMA-based actuator. Section III discusses the experimental characterization of the actuator. Section IV describes the development and functionality of the MiniBug and WaterStrider platforms, which we created to test and demonstrate the capabilities of the actuator. Lastly, Section V draws some conclusions regarding the presented research.

II. Design and Fabrication

The dynamic behavior of an SMA wire is characterized by the *shape memory effect* (SME) and the *superelasticity* property [16]. These phenomena are observable when the SMA material composing the wire transitions between three distinct crystal-structure phases: *detwinned martensite*, *twinned martensite*, and *austenite*. As shown in Fig. 2(a), an actuation cycle can be induced through sequential heating, cooling, and application of stress. The proposed design can be driven using *Joule* heating [17], or other methods such as catalytic combustion [15], and passive cooling (free convection); stress is continuously applied using a leaf spring made of *carbon fiber* (CF), as shown in Fig. 2(b). In this specific case, the SMA material (nitinol), under a stress of 172 MPa, has a nominal transition temperature from martensite to austenite of 90 °C. Using basic beam theory, it can be shown that the force applied by the leaf spring is approximately constant for contractions of the actuator's SMA wires greater than 18 µm; therefore, for design purposes, we assumed that the stress experienced by the SMA material remains constant during an entire actuation cycle. As seen in Fig. 3, from a fabrication viewpoint, the proposed SMA-based actuator is composed of three main types of components: (i) two parallel 25.4-µm-diameter SMA wires (Dynalloy Flexinol HT SMA Wire); (ii) a 90-µm-thick CF beam, made of Tenax 112 prepreg, that functions as a leaf spring; and, (iii) two cross-shaped plates, made of copper-clad FR4 (Cu-FR4), used for electrical and mechanical connection.

Using data reported in [13] and simple mechanical tests, we chose a thickness of 90 µm, a width of 0.5 mm, and a length of 6 mm for the CF beam in order to heuristically minimize weight and maximize actuator output at high frequencies. Similarly, we chose the smallest commercially-available diameter of 25.4 µm for the SMA wires in order to minimize the volume with respect to the surface of the SMA material, thus maximizing the free-convection rate of cooling. In this case, the design trade-off is that the force produced by an SMA wire decreases with its diameter. To compensate, we can simply increase the number of SMA wires used for actuation; as already mentioned, the presented design uses two in parallel. All the steps in the simultaneous fabrication process of four actuators are detailed in Fig. 3(a). In Step 1, a Cu-FR4 frame is cut using a 3-W 355-nm DPSS laser

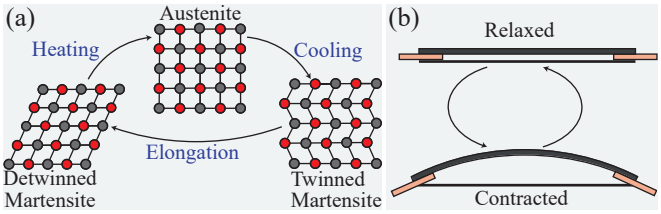

Fig. 2. **Design and functionality of the proposed SMA-based actuator. (a)** Depiction of the molecular crystal structure of an SMA material during cycles of heating and cooling, assuming the completion of major hysteretic loops. In the case of an SMA wire, starting at the elongated *detwinned martensite* phase, the SMA material reaches the *austenite* phase after the application of sufficient heat to surpass the SMA transition temperature and thus force the contraction of the wire according to the *shape-memory effect* (SME). Then, after sufficient cooling, the material transitions to the *twinned martensite* phase. As shown, the application of an external stress detwins the SMA material and the wire elongates until reaching its initial state. **(b)** Depiction of a complete SME-based actuation cycle during operation. Heat is applied to the SMA wire using *Joule* heating; cooling of the SMA material occurs passively through unforced convection; simultaneously, the SMA material is detwinned using a CF leaf spring.

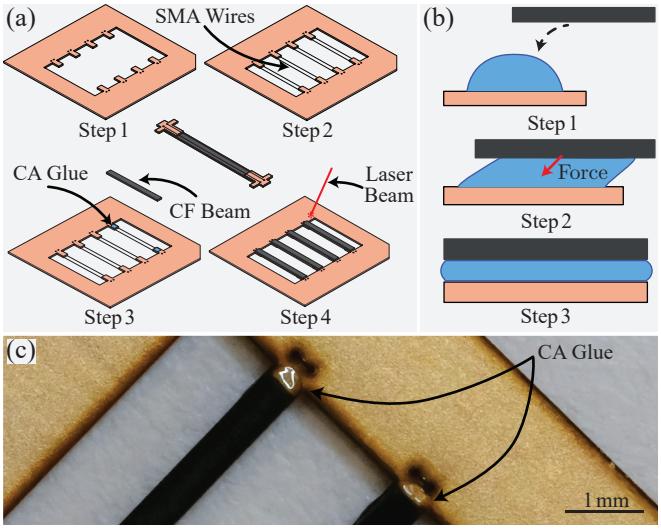

Fig. 3. **Fabrication of the proposed SMA-based actuator. (a)** Steps of the SCM-based fabrication procedure. In Step 1, a 3-W 355-nm DPSS laser (Photonics Industries DCH-355-3) is used to micromachine the Cu-FR4 supporting frame employed during fabrication. In Step 2, SMA wires are looped through holes in the frame, and secured under tension with a simple knot and a small amount of CA glue (Loctite 401). In Step 3, we use capillary self-alignment to accurately place four CF beams onto premachined alignment tabs of the Cu-FR4 frame. In Step 4, the actuator is released from the Cu-FR4 frame using a 3-W 355-nm DPSS laser. **(b)** Capillary alignment used in Step 3 of the actuator fabrication process. In Step 1, droplets of CA glue are precisely placed onto alignment tabs of the Cu-FR4 frame, and four CF beams are immediately placed on top of the droplets. In Step 2, each beam is pulled, without external intervention, in the desired direction of alignment due to the surface tension of the glue and capillary action at the beam-glue interface. In Step 3, the CA glue cures and the CF beams become precisely aligned over the tabs of the Cu-FR4 frame. **(c)** Photo showing two cured CA glue droplets and two precisely aligned beams after completion of Step 3 in the actuator fabrication process.

(Photonics Industries DCH-355-3). In Step 2, SMA wires are looped through orifices at two opposite sides of the Cu-FR4 frame and tied under tension using a simple knot; then, they are secured using a small amount of *cyanoacrylate* (CA) glue (Loctite 401). In Step 3, CF beams are installed on protrusions (alignment tabs) of the frame, using the passive capillary self-alignment phenomena described in [18], [19]; at this scale, the properties of the chosen CA glue produce the

capillary effects necessary for passive self-alignment during the short period of time before curing.

The mechanism of the capillary-alignment technique is depicted in Fig. 3(b). First, droplets of CA glue are precisely deposited on the alignment tabs of the Cu-FR4 frame; then, premachined CF beams are placed on top of the droplets; lastly, with proper droplet placement, the capillary forces of the CA glue *pull* the CF beams perfectly over the Cu-FR4 alignment tabs before the glue cures. Because of the quick cure time of CA glue, the CF beams must be placed immediately after droplet deposition to ensure proper capillary alignment. Specifically, the beams are passively aligned on the Cu-FR4 tabs with respect to their transverse direction while slight manipulations with tweezers are required to center them with respect to their axial direction. In Step 4, as depicted in Fig. 3(a), the actuators are released using DPSS laser cutting. The photograph in Fig. 3(c) shows a close-up of an actuator-fabrication frame after the installation of CF beams; here, the precise alignment of two beams on their Cu-FR4 tabs can be seen as well as the cured CA glue droplets holding them in place.

III. Actuator Characterization

A. Experimental Setup

For the experimental characterization of the proposed actuator dynamics, we used the setup shown in Fig. 4. As seen in the signals-and-systems diagram of Fig. 4(a), a MathWorks Simulink Real-Time system is used to generate the *pulse-width-modulation* (PWM) voltage signal with pre-specified characteristics—frequency, *on*-voltage height, and *duty cycle* (DC)—that drives the actuator. The power of this PWM signal is amplified with a MOSFET-based circuit (YYNMOS-4) to provide sufficient current to Joule heat the SMA wires during actuation. Throughout characterization, the tested actuator is mounted on the stand shown in Fig. 4(b) and depicted in Fig. 4(c). In this configuration, one end of the actuator is attached to a 3D-printed mount while the other end is precisely aligned below a laser displacement sensor (Keyence LK-G32) to measure the instantaneous displacement output of the actuator. During the tests, signals are digitally generated, measured variables are read and recorded, and information is processed at a rate of 10 kHz.

During one PWM period, the voltage applied across an SMA wire of the actuator is first *on*, then *off*; here, *on* corresponds to 15 V and *off* corresponds to 0 V. The contraction rate of an SMA wire directly depends on the amount of current running through it [13], [17], and the DC of the driving PWM signal—defined as the fraction of the signal period for which the signal is in the *on* state—determines the fraction of time an actuator is allowed to heat during a PWM cycle [13]. At low operation frequencies ($\sim$1 Hz), a large DC might result in the SMA material becoming overheated and damaged. Therefore, using information from simple tests, we selected a set of DC values for each considered frequency. We chose an *on*-voltage height of 15 V to limit the current passing through the SMA wires of the actuator to 200 mA. This limitation is critical to avoid overheating and damaging the SMA material and thin copper wires (52 AWG) used to connect the actuator to the driving power circuit.

To empirically evaluate the performance of an actuator regarding force and work, we load and operate it with several

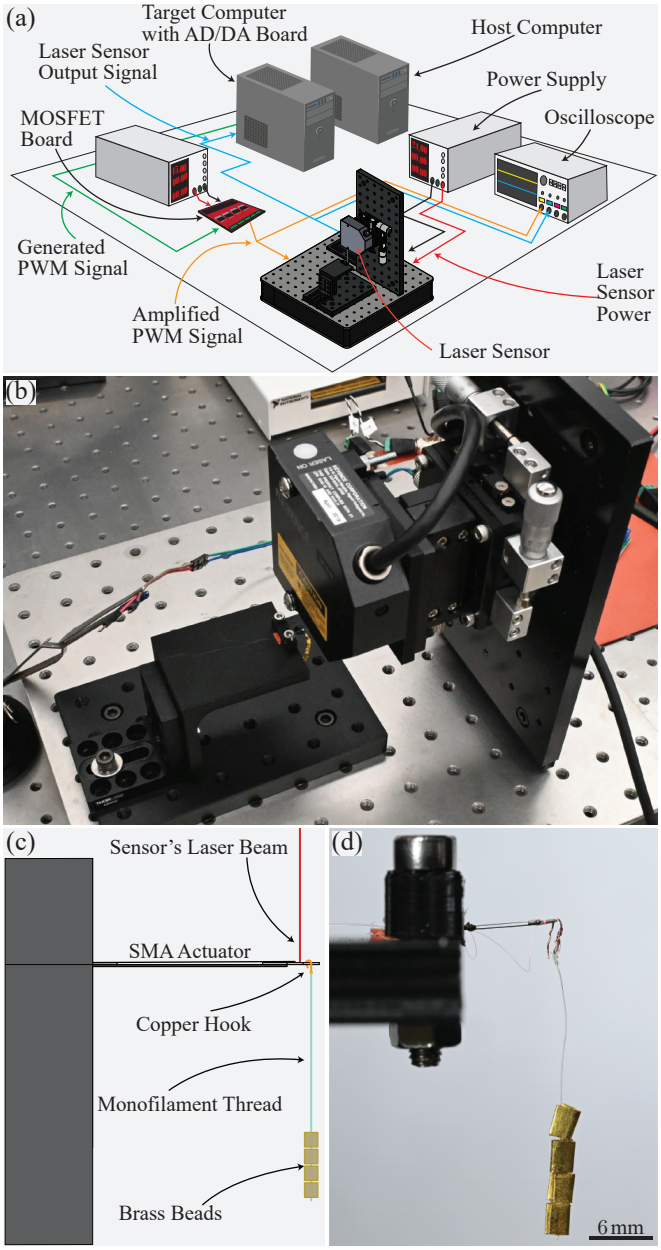

Fig. 4. **Experimental setup used to dynamically characterize the proposed actuator**. **(a)** Signals-and-systems diagram of the setup. A MathWorks target-and-host Simulink Real-Time system with a National Instruments PCI-6229 AD/DA board is used to digitally generate signals, read and record measured variables, and process information at a rate of 10 kHz. Accordingly, the PWM signal required to excite the tested actuator is first generated and then its power is amplified with a MOSFET-based circuit (YYNMOS-4) to provide sufficient current while *Joule* heating the SMA wires of the tested actuator. A laser displacement sensor (Keyence LK-G32) measures the instantaneous deflection of the actuator's tip, the output. An oscilloscope monitors signals in real time and records the PWM data coming from the MOSFET-based circuit. **(b)** Photograph of the test stand with an actuator mounted. **(c)** Schematic of the weight-loading method and fixture used to hold an actuator during the characterization tests. The tested actuator is fixed on one end with the distal free end precisely aligned, using a 3-axis optomechanical stage, under the laser displacement sensor shown in (b). We use a copper hook to attach a piece of monofilament thread to the actuator; we secure it with a small amount of CA glue. We increase the loading acting on the actuator by crimping additional brass beads, weighing 0.18 mN each, to the thread. After they are crimped, the beads are secured using CA glue to prevent shaking during operation. To compensate for the 0.015-mN weight of the hook and thread, the first crimped bead weighs only 0.165 mN. **(d)** Photo of a tested actuator mounted on the experimental stand with a 0.72 mN load hanging from it.

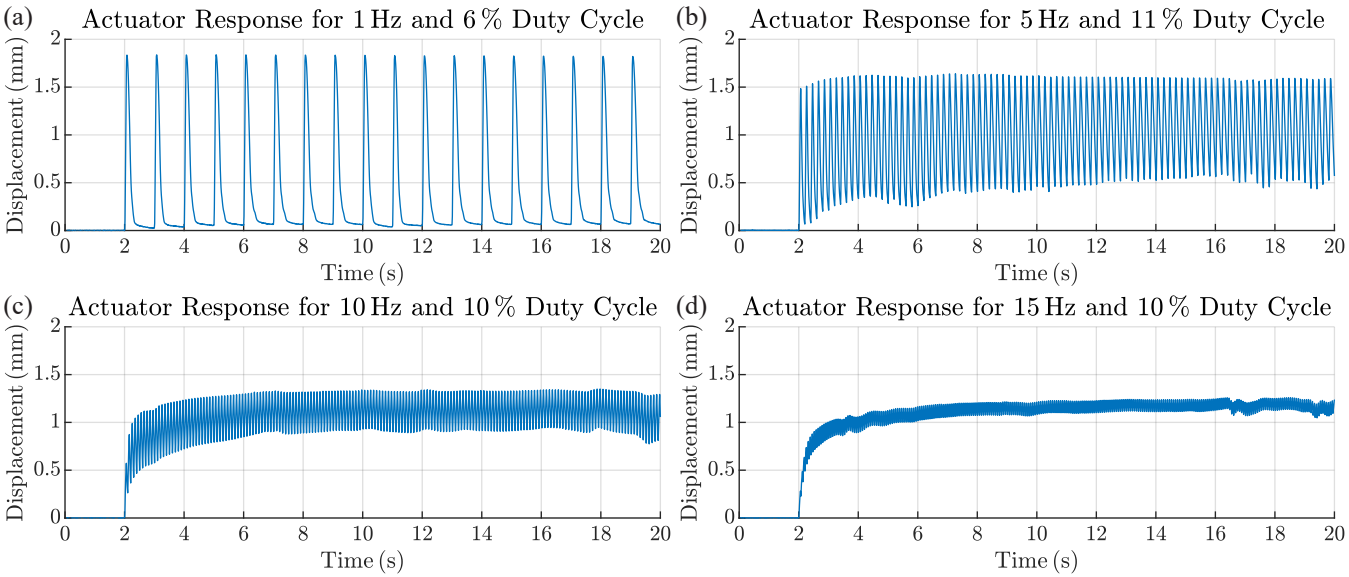

Fig. 5. **Actuator responses measured with a laser displacement sensor. (a)** Actuator response to a PWM signal with a frequency of 1 Hz and DC of 6 %. **(b)** Actuator response to a PWM signal with a frequency of 5 Hz and DC of 11 %. **(c)** Actuator response to PWM signal with a frequency of 10 Hz and DC of 10 %. **(d)** Actuator response to a PWM signal with a frequency of 15 Hz and DC of 10 %. In these four cases, the *on*-voltage height of the PWM signal is 15 V.

different weights for several different PWM parameters. Figs. 4(b)–(d) graphically describe the method to load the actuator. As seen, a short piece of monofilament thread is connected to the distal end of the actuator through a copper hook; then, brass beads weighing 0.18 mN each are incrementally crimped onto the thread until the actuator can no longer lift the load. To compensate for the combined 0.015-mN weight of the hook and thread, the first bead was chosen to weigh only 0.165 mN. After data collection, the displacement data measured with the laser sensor is processed offline using a zero-phase low-pass filter—designed with MATLAB's digital-filter-design tool—to reduce sensor noise. We then employ simple algorithms run in MATLAB to compute figures of merit to evaluate the performance of the proposed actuator.

B. Characterization Results

Actuator responses for PWM exciting frequencies of 1, 5, 10, and 15 Hz are shown in Figs. 5(a)–(d), respectively. As indicated in the plots, the associated DC values are 6, 11, 10, and 10 %, which were empirically determined to maximize actuator output. Sections of these experiments can be seen in the accompanying supplementary movie. At 1 Hz, the measured steady-state deflection at the actuator's tip oscillates between about 0.1 and 1.75 mm, which approximately corresponds to a major hysteretic loop [16]. At higher frequencies, the amplitude of oscillation decreases and a steady-state deflection offset occurs. These phenomena result from the hysteretic behavior of the SMA material during heating-and-cooling cycles, and the limited time available for the SMA wires to cool down and reach ambient temperature. To evaluate actuator performance, we define the *maximum actuator displacement output* (MADO) for an actuation cycle as the difference between the maximum and minimum beam deflection at the actuator's tip during a PWM period, measured using the laser sensor shown in Fig. 4(b). Furthermore, for a test defined by its PWM exciting frequency and PWM DC value, we define the *average* MADO (AMADO) as the mean of the MADO sequence for a test, computed across 15 s of steady-state data. Fig. 6(a) shows the AMADO values corresponding to all sixty experimental cases defined by the exciting PWM frequencies in the set $\{1, 5, 10, 15\}$ Hz and PWM DC values in the set $\{1, 2, 3, 4, 5, 6, 7, 8, 9, 10, 11, 12, 13, 14, 15\}$ %. For plotting and analysis purposes, for each PWM frequency, we normalized the AMADO data by dividing them by the maximum computed AMADO value among all the tested DC values. As mentioned above, for the elements in the chosen frequency set, these maxima respectively occur when the DC values are chosen to be 6, 11, 10, and 10 %; correspondingly, the specific maximum raw AMADO values are 1.625, 1.15, 0.48, and 0.14 mm. As seen, the AMADO value for an experiment significantly decreases as the exciting PWM frequency increases; however, at 15 Hz, the AMADO value of 140 µm is still comparable to the displacement a piezoelectric actuator of this scale can produce [20].

During force-output characterization experiments, for each PWM exciting frequency, we employ the DC value corresponding to the largest load-free AMADO value. In the cases presented here, for each load in the set $\{0, 0.18, 0.36, 0.54, 0.72, 0.90, 1.08, 1.26, 1.44\}$ mN and each frequency in the set $\{1, 5, 10, 15\}$ Hz, we measured the instantaneous loaded deflection, $d_{\max}(f_{\text{load}})$, of the actuator's tip and compute the *average loaded* MADO (ALMADO) value across 15 s, $\bar{d}_{\max}(f_{\text{load}})$, where f_{load} is the corresponding load. The chosen load set is a reflection of the way we increment the weight of the test load in each sequential experiment. Specifically, in a first set of experiments, the actuator is excited unloaded; then, in a second set of experiments, we add a weight of 0.18 mN, corresponding to the hook, the monofilament thread, and a 0.165-mN brass bead; then, in a third set of experiments, we crimp a 0.18-mN bead to the thread, and so forth, as depicted in Figs. 4(c)–(d). We determined empirically that eight brass

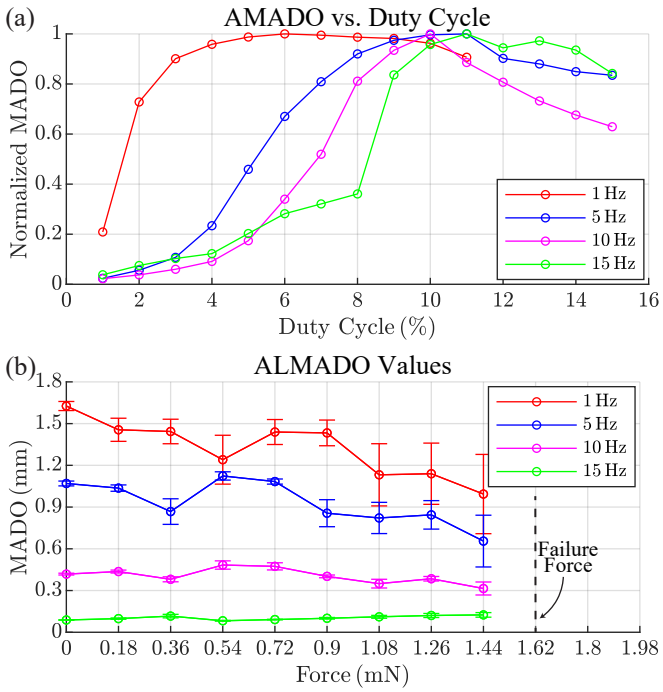

Fig. 6. **Normalized *average* MADO (AMADO) and *average loaded* MADO (ALMADO) values measured experimentally**. **(a)** AMADO values corresponding to all sixty cases defined by the exciting PWM frequencies in the set $\{1, 5, 10, 15\}$ Hz and PWM DC values in the set $\{1, 2, 3, 4, 5, 6, 7, 8, 9, 10, 11, 12, 13, 14, 15\}$ %. At 1 Hz, the largest AMADO value of 1.625 mm corresponds to a DC of 6 %. At 5 Hz, the largest AMADO value of 1.15 mm corresponds to a DC of 11 %. At 10 Hz, the largest AMADO value of 0.48 mm corresponds to a DC of 10 %. At 15 Hz, the largest AMADO value of 0.14 mm corresponds to a DC of 10 %. During the performance of these experiments, the measured ambient temperature oscillated approximately two degrees about 22 °C. **(b)** ALMADO data corresponding to all thirty-six cases defined by the exciting PWM frequency-DC pairs in the set $\{\{1\,\text{Hz}, 6\,\%\}, \{5\,\text{Hz}, 11\,\%\}, \{10\,\text{Hz}, 10\,\%\}, \{15\,\text{Hz}, 10\,\%\}\}$ and the loads in the set $\{0, 0.18, 0.36, 0.54, 0.72, 0.90, 1.08, 1.26, 1.44\}$ mN. Each data point in the plot denotes the mean of the ALMADO values obtained through five different back-to-back experiments. The associated *standard error of the mean* (SEM) values are indicated with vertical bars. For each tested load, the ALMADO value significantly decreases as the exciting frequency increases. Also, for the first three frequencies, a decreasing trend of the ALMADO value, as the load increases, can be observed. Namely, for the pair $\{1\,\text{Hz}, 6\,\%\}$, the mean of this figure of merit decreases from 1.625 to 0.994 mm. Similarly, for the pair $\{5\,\text{Hz}, 11\,\%\}$, it decreases from 1.15 to 0.655 mm; and, for the pair $\{10\,\text{Hz}, 10\,\%\}$, from 0.48 to 0.315 mm. In contrast, for the pair $\{15\,\text{Hz}, 10\,\%\}$, the ALMADO value remains approximately constant as the load increases.

beads (corresponding to 1.44 mN) can be added before an actuator of the considered type fails.

The mean and *standard error of the mean* (SEM) of the ALMADO values obtained through five different experiments, for each considered frequency and DC value, are shown in Fig. 6(b). Using these data, we can estimate the *average maximum actuator work output* (AMAWO) as a function of the loading force for each frequency by computing $\overline{W}_{\max}(f_{\text{load}}) = f_{\text{load}} \cdot \bar{d}_{\max}(f_{\text{load}})$. For a frequency of 1 Hz, the best observed AMAWO value is of 1.4 µJ, which corresponds to a load of 1.26 mN. Clearly, for each tested load, the ALMADO value significantly decreases as the exciting frequency increases. Also, despite the existence of several outliers, for the first three frequencies, the data in Fig. 6(b) indicates a decreasing trend of the ALMADO value as the load increases. Specifically, for

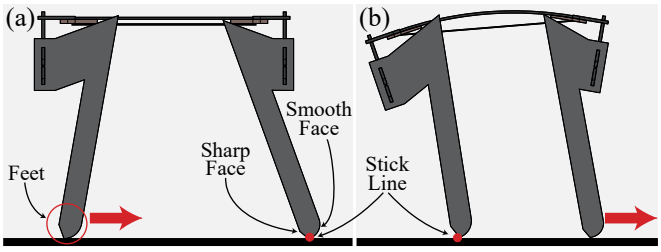

Fig. 7. **Design and functionality of the MiniBug. (a)** The MiniBug in its expanded state. The feet of this robot were designed with a sharp face and a smooth face to generate anisotropic friction and, as a consequence, forward locomotion during cyclic operation of the driving actuator. As the SMA wires of the driving actuator contract during heating, the sharp faces of the robot's front feet anchor to the supporting surface while the rear feet slide forward. **(b)** The MiniBug in its contracted state. As the SMA wires of the driving actuator elongate during cooling, the sharp faces of the robot's rear feet anchor to the supporting surface while the front feet slide forward.

the frequency-DC pair $\{1\,\text{Hz}, 6\,\%\}$, the mean of this figure of merit decreases from 1.625 to 0.994 mm. Similarly, for the pair $\{5\,\text{Hz}, 11\,\%\}$, it decreases from 1.15 to 0.655 mm; and, for the pair $\{10\,\text{Hz}, 10\,\%\}$, from 0.48 to 0.315 mm. In contrast, for the pair $\{15\,\text{Hz}, 10\,\%\}$, the ALMADO value remains approximately constant as the load increases. It is not clear why this phenomenon occurs, but it might be related to the amount of kinetic energy in the system as a whole. Note that both the relatively large SEM values and output variations due to load increases highlight the need for feedback control in real-time applications of actuators of this type. Actuator failure typically occurs at a load of about 1.6 mN and, using simple microscopic analyses, we determined that this is caused by the fracture of the SMA material under mechanical stress. Also, the cause of failure provides empirical evidence of the structural integrity and high functionality of the proposed actuator. Consistently, its outstanding strength and work density are also evidenced by its ability to lift 155 times its own weight for all the tested frequencies. To our best knowledge, no other microactuation technology compares to the presented method regarding work density. To further demonstrate these capabilities, in Section IV, we present two mobile microrobots driven by this actuation method.

IV. Applications in Microrobotics

A. The MiniBug

With a total weight of 8 mg and a length of 8.5 mm, the MiniBug (see Fig. 1) is the lightest fully-functional SMA-driven crawler reported to date. This platform compellingly demonstrates the high-frequency capabilities of the proposed 0.96-mg SMA-based actuator and its suitability to be integrated into microrobots. The MiniBug's base design was inspired by the SMALLBug presented in [13]. However, a new slot-and-pin alignment method, along with a tuning procedure for its final physical configuration, enabled us to use 90-µm-thick CF material, which resulted in a significantly smaller and lighter robotic structure. We designed the feet of the MiniBug to cyclically and coordinately produce anisotropic friction and, as a consequence, forward locomotion. Each of the four feet has a sharp and a smooth face of contact with the supporting ground. Fig. 7 depicts the locomotion mechanisms during operation. Theoretically, as depicted in Fig. 7(a), during heating, the actuator contracts

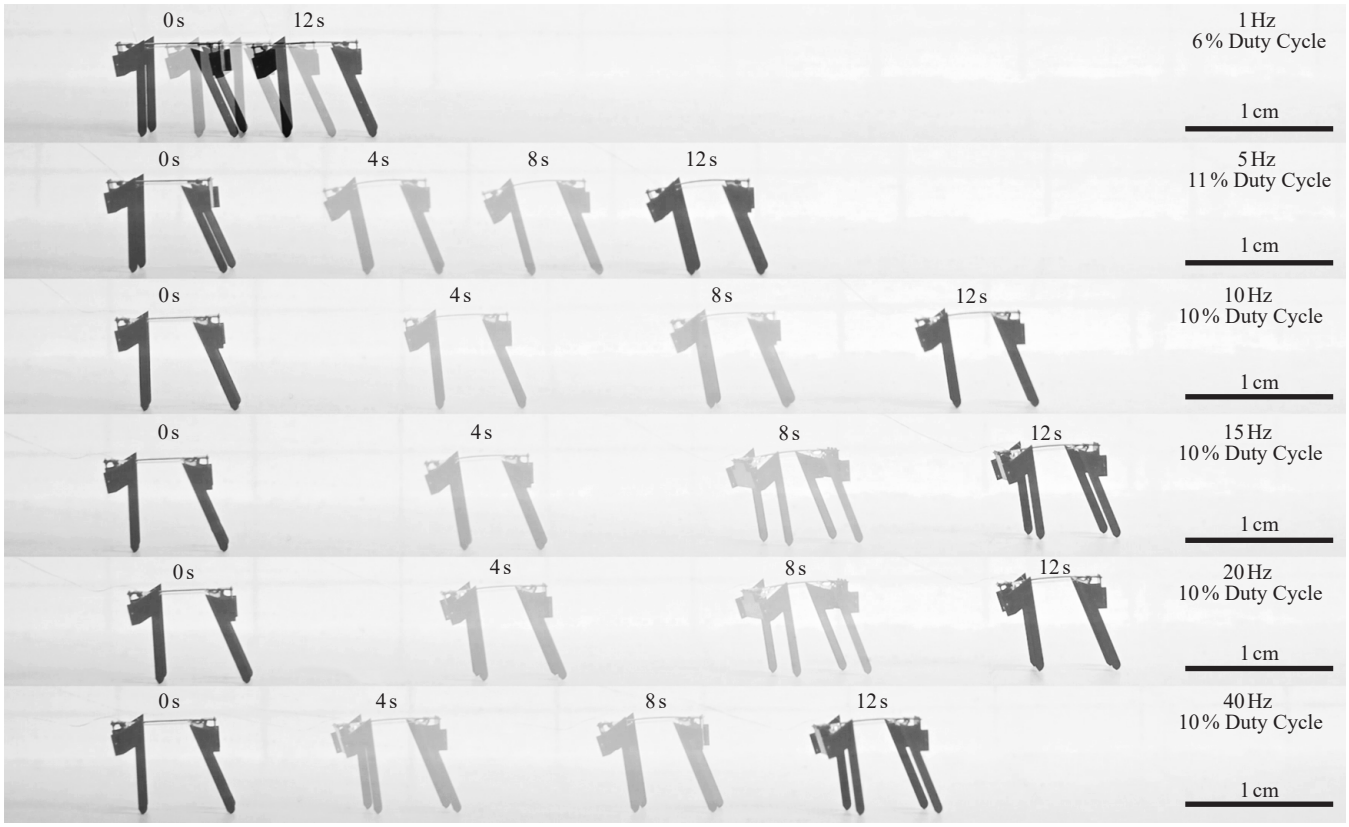

Fig. 8. **The MiniBug locomoting at six different actuation frequencies.** The photographic sequences show the distance traveled by the MiniBug at intervals of 4 s, for the operation frequencies in the set $\{1, 5, 10, 15, 20, 40\}$ Hz; the DC values are the empirical optima determined according to the method discussed in Section III. The fastest relative speed of 0.76 BL/s occurs at 15 Hz. Depending on the frequency of operation, the robot exhibits four locomotion modes: (i) *crawling*, (ii) *shuffling*, (iii) *galloping*, and (iv) *gliding*. At 1 Hz, the MiniBug slowly crawls, achieving an average speed of 0.10 BL/s; at 5 Hz, the locomotion mode changes to shuffling, during which the MiniBug achieves an average speed of 0.46 BL/s; at 10 Hz, 15 Hz, and 20 Hz, the locomotion mode switches to galloping, during which the MiniBug achieves average speeds of 0.69 BL/s, 0.76 BL/s, and 0.75 BL/s, respectively. At the highest frequency of 40 Hz, the MiniBug *glides* and hardly any actuator output displacement can be noticed as high-frequency vibrations allow the robot to *virtually* float forward at an average speed of 0.61 BL/s. Video footage of these tests can be seen in the accompanying supplementary movie.

and the front feet anchor to the ground as the stick lines of their sharp faces cling to the supporting surface while the back feet slide toward the right on their smooth faces. This contraction also moves the robot's *center of mass* (COM) closer to the back legs, thus increasing the normal force acting on the back feet while anchored to the ground and facilitating the forward sliding of the front feet as the actuator expands during cooling, as shown in Fig. 7(b). In reality, during crawling, the robot's feet slightly slide when they are supposed to be completely anchored; this phenomenon is more prominent at low locomotion frequencies (1 Hz). This issue is mitigated at higher frequencies because the deflection drift of the driving actuator keeps the COM closer to the rear legs, which reduces undesired back sliding and, as a consequence, increases crawling efficiency.

To test and demonstrate the locomotion capabilities of the robot, we simply excited the driving actuator, in open loop, using a PWM signal with constant parameters during operation. As shown in Fig. 8, we tested six cases corresponding to the frequency-DC pairs: $\{1\,\text{Hz}, 6\,\%\}$, $\{5\,\text{Hz}, 11\,\%\}$, $\{10\,\text{Hz}, 10\,\%\}$, $\{15\,\text{Hz}, 10\,\%\}$, $\{20\,\text{Hz}, 10\,\%\}$, and $\{40\,\text{Hz}, 10\,\%\}$. In all these tests, we kept the PWM *on*-voltage height at 18 V, which we calculated using the total resistance of the actuator system in order to limit the resulting current to 200 mA. The photo sequences in Fig. 8 show 12 s of locomotion corresponding to the six experiments. Video footage of these tests can be seen in the accompanying supplementary movie. The MiniBug exhibits the same locomotion modes of the SMALLBug discussed in [13]; however, at the highest actuation frequency of 40 Hz, a new locomotion mode is observed, which we dubbed as *gliding*. In this mode, the driving actuator does not display noticeable actuator deflections; we speculate that the generated high-frequency vibrations induce the robot to slide forward. Because of the manner locomotion is produced at high frequencies, in this mode, traction is not significant and the MiniBug can be easily pushed around by minor disturbances. Everything considered, the best locomotion performance is achieved at the actuation frequency of 15 Hz because the robot simultaneously generates significant traction and locomotes at its fastest speed of 0.76 BL/s. In all tested modes, due to its small mass, the MiniBug is subjected to relatively large forces from the tether wires, which heavily affect locomotion speed. To remove these disturbances, we envision a tetherless power solution based on either directed-energy transmission, or catalytic combustion.

B. The WaterStrider

The extraordinary physical abilities exhibited by water-surface-tension locomoting insects have inspired

scientific research [21], [22] and the development of new robots, such as those presented in [23] and [24]. The robot in [23] weighs 1 g, stays afloat on hydrophobic wires, and uses sophisticated actuation mechanisms to generate elliptical stroke patterns for locomotion. However, its weight is much larger than that of *Aquarius paludum* specimens used for inspiration, which have a mass of only about 20 mg. The robot in [24] weighs 68 mg, stays afloat on hydrophobic wires, and can jump vertically 142 mm. In this case, SMA wires provide the actuation forces needed to jump off the water; however, this robot was not reported capable of locomotion. With a weight of 56 mg and a length of 22 mm, the WaterStrider (see Fig. 1) is the lightest controllable water-surface-tension locomoting robot reported to date. We designed this robot to efficiently utilize the large force outputs produced by the unimorph SMA-based actuator presented in Section III. The weight of the robot is supported by elliptical feet designed with large surface areas to exploit surface-tension forces while standing on water. We also designed the highly-flexible fin-like propulsor depicted in Fig. 9(a) to take advantage of fluid-structure-interaction phenomena and thus increase hydrodynamic efficiency; actuating each propulsor independently enables locomotion and turning capabilities.

We used the modified SCM method in [15] to fabricate all the structural and functional components of the WaterStrider, including two four-bar transmissions, four elliptical feet, a body frame, two fin-like propulsors (see Fig. 1), and two SMA-based actuators of the type discussed in Section III. Consistently, all these multi-layer parts were made from 90-µm-thick CF sheets and Kapton film. For the final assembly, we used the method presented in [15] and the capillary alignment technique discussed in Section II. A key structural element of the WaterStrider's body frame are twisting reinforcement bars, installed to prevent actuation-induced body warping during operation. The main locomotion mode designed for the WaterStrider is depicted in Figs. 9(b)–(d). Here, the two four-bar transmission mechanisms receive as inputs the displacement outputs generated by the two SMA-based actuators and amplify them into large stroke-angle outputs that drive the fin-like bending propulsors of the system. As seen, during a locomotion period, the two actuators contract and then relax, enabling the propulsors to provide the force necessary to push the WaterStrider forward. During forward locomotion, both actuators are operated symmetrically, in open loop, to generate a large straight propulsion force. Accordingly, to execute turning maneuvers, one actuator-propulsor pair is actuated with a 5-Hz PWM signal while the other actuator-propulsor pair is left inactive, which produces a drag-based turning torque on the robot.

The photographic sequences in Fig. 10 summarize the experiments performed to test and demonstrate the locomotion capabilities of the WaterStrider. Video footage of these tests can be seen in the accompanying supplementary movie. The sequence in Fig. 10(a) shows the WaterStrider during forward locomotion in open loop. In this case, both driving actuators were excited using 1-Hz PWM signals with the optimal DC of 6 %, empirically determined through the characterization experiments discussed in Section III. We selected an *on*-voltage height of 12 V to ensure that no more than 200 mA of current passed through the SMA

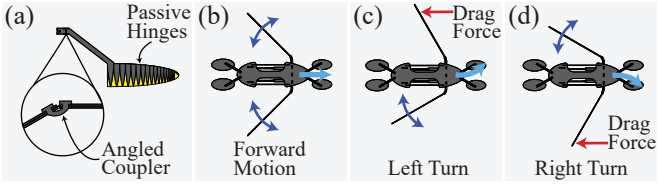

Fig. 9. **Design and functionality of the WaterStrider. (a)** The fin of the propulsor was designed to be flexible with a structure composed of a series of hinges, made of CF and Kapton, and fabricated using the SCM method. The robot was designed with its two propulsors biased towards the back of its body in order to reduce drag during forward locomotion. This characteristic was achieved using rigid 30-degree angled couplers that connect, through CF bars, the transmissions and fins of the two propulsors. The couplers can be replaced to change the inclination angles of the propulsors. **(b)** To generate forward thrust and, as a consequence, forward locomotion, the WaterStrider symmetrically flaps its two propulsors cyclically. **(c)** To turn left, the WaterStrider flaps its right fin-like propulsor at a frequency of 5 Hz while its left propulsor remains inactive. The asymmetrical production of thrust plus the drag force acting on the inactive left propulsor generate a functional counter-clockwise torque on the robot's body. **(d)** To turn right, the WaterStrider flaps its left fin-like propulsor at a frequency of 5 Hz while its right propulsor remains inactive. The asymmetrical production of thrust plus the drag force acting on the inactive right propulsor generate a functional clockwise torque on the robot's body.

wires of the actuators; the same *on*-voltage height was kept in all the experiments shown in Fig. 10. With these excitation parameters, the WaterStrider achieved an average speed of 0.26 BL/s. The sequence in Fig. 10(b) also shows the WaterStrider during forward locomotion in open loop. In this case, however, both driving actuators were excited using 2-Hz PWM signals with a DC of 7.5 %. With these excitation parameters, the WaterStrider achieved an average speed of 0.28 BL/s.

To execute turning maneuvers, such as those shown in Figs. 10(c)–(d), one actuator-propulsor pair is open-loop excited using a 5-Hz PWM signal with the optimal DC of 11 %, determined through the characterization tests described in Section III, while the other actuator-propulsor pair is left inactive to produce a drag-induced body torque, as already explained. Specifically, in the test shown in Fig. 10(c), the right actuator-propulsor pair is excited to make the robot turn left; similarly, in the test shown in Fig. 10(d), the left actuator-propulsor pair is excited to make the robot turn right. During these left and right turning maneuvers, the WaterStrider achieved rates of 0.144 and 0.073 rad/s, respectively. It is important to mention that the forces exerted by the tether wires on the WaterStrider during operation significantly affect its locomotion behavior because the friction induced by the water surface is almost negligible. For the same reason, the locomotion trajectory of its body can be easily and heavily disturbed by other external forces; this fact explains the observed difference in angular speed when the robot turns right and left. The ability of the WaterStrider to overcome these disturbances, while executing forward locomotion and turning maneuvers, demonstrates the capacity of the proposed SMA-based actuators to produce high output forces. Furthermore, these results indicate that once new onboard, or tetherless, technologies become available to power microrobots of the WaterStrider type, a wide gamut of applications useful for humans will become a reality. The most promising possibilities are high-density batteries [2], catalytic combustion [15], and directed transmission of electromagnetic energy [12].

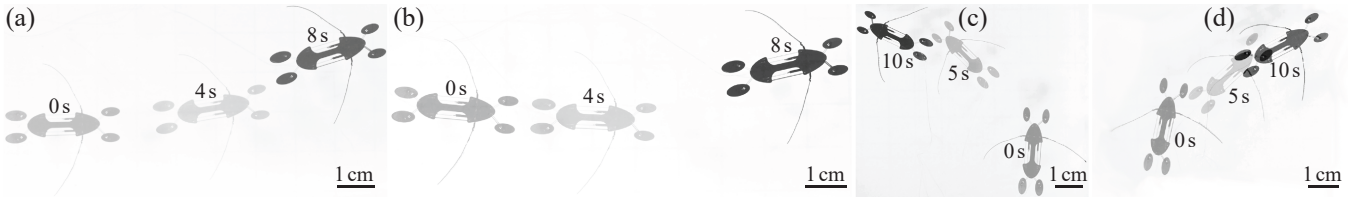

Fig. 10. **The WaterStrider locomoting on water. (a)** Photographic sequence showing the robot moving forward at an actuation PWM frequency of 1 Hz. The photographs in the composite were taken at 0, 4, and 8 s. **(b)** Photographic sequence showing the robot moving forward at an actuation PWM frequency of 2 Hz. The photographs in the composite were taken at 0, 4, and 8 s. **(c)** Photographic sequence showing a left turn. To execute this maneuver, the WaterStrider flaps its right fin-like propulsor at a PWM frequency of 5 Hz while its left propulsor remains inactive. The photographs in the composite were taken at 0, 5, and 10 s. **(d)** Photographic sequence showing a right turn. To execute this maneuver, the WaterStrider flaps its left fin-like propulsor at a PWM frequency of 5 Hz while its right propulsor remains inactive. The photographs in the composite were taken at 0, 5, and 10 s. Video footage of these tests can be seen in the accompanying supplementary movie.

V. Conclusions

We presented a new 0.96-mg ($\sim$1 mg) fast unimorph SMA-based actuator that is capable of high-frequency operation (up to 40 Hz) as well as lifting 155 times its own weight. This development is the result of using the modified SCM method in [15], [20] and the introduction of a new alignment technique for microfabrication based on the use of passive capillary forces. Through dynamic characterization experiments, we tested and demonstrated the high-frequency operation and high-force output capabilities of the proposed SMA-based actuator. To show the suitability of the actuator in microrobotic applications, we designed and built two locomoting microrobots: (i) the MiniBug, which, with a weight of 8 mg and a length of 8.5 mm, is the lightest fully-functional SMA-driven terrestrial crawler reported to date; and, (ii) the 56-mg 22-mm–long WaterStrider, which is the first subgram controllable SMA-driven crawler capable of locomoting on water by taking advantage of surface-tension effects. Through the discussion of several tests, we demonstrated the locomotion behavior and performance of the MiniBug during operation, which can function at actuation frequencies of up to 40 Hz and achieve an average speed of 0.76 BL/s. Similarly, we demonstrated the locomotion behavior and performance of the WaterStrider during operation, which can achieve an average speed of 0.28 BL/s and execute turning maneuvers at angular rates of up to 0.144 rad/s. To achieve autonomy, we envision the deployment of MiniBug and WaterStrider platforms in swarms that collectively would be capable of carrying enough power to complete missions.

References

[1] D. Lee, S. Kim, Y.-L. Park, and R. J. Wood, "Design of Centimeter-Scale Inchworm Robots With Bidirectional Claws," in *Proc. IEEE Int. Conf. Robot. Automat. (ICRA)*, Shanghai, China, May 2011, pp. 3197–3204.

[2] B. Goldberg, R. Zufferey, N. Doshi, E. F. Helbling, G. Whittredge, M. Kovac, and R. J. Wood, "Power and Control Autonomy for High-Speed Locomotion With an Insect-Scale Legged Robot," *IEEE Robot. Automat. Lett.*, vol. 3, no. 2, pp. 987–993, Apr. 2018.

[3] Y. Wu, J. K. Yim, J. Liang, Z. Shao, M. Qi, J. Zhong, Z. Luo, X. Yan, M. Zhang, X. Wang, R. S. Fearing, R. J. Full, and L. Lin, "Insect-Scale Fast Moving and Ultrarobust Soft Robot," *Sci. Robot.*, vol. 4, no. 32, Jul. 2019, Art. no. eaax1594.

[4] W. Zhou and N. Gravish, "Soft Microrobotic Transmissions Enable Rapid Ground-Based Locomotion," in *Proc. IEEE/RSJ Int. Conf. Intell. Robots Syst. (IROS)*, Las Vegas, NV, USA, Oct. 2020, pp. 7874–7880.

[5] S. Hollar, A. Flynn, C. Bellew, and K. S. J. Pister, "Solar Powered 10 mg Silicon Robot," in *Proc. 16th Int. Conf. Micro Electro Mech. Syst. (MEMS)*, Kyoto, Japan, Jan. 2003, pp. 706–711.

[6] D. S. Contreras, D. S. Drew, and K. S. J. Pister, "First Steps of a Millimeter-Scale Walking Silicon Robot," in *Proc. 19th Int. Conf. Solid-State Sens. Actuators Microsyst. (TRANSDUCERS)*, Kaohsiung, Taiwan, Jun. 2017, pp. 910–913.

[7] D. Vogtmann, R. St. Pierre, and S. Bergbreiter, "A 25 mg Magnetically Actuated Microrobot Walking at $>$ 5 Body Lengths/sec," in *Proc. 30th Int. Conf. Micro Electro Mech. Syst. (MEMS)*, Las Vegas, NV, USA, Jan. 2017, pp. 179–182.

[8] H. Lu, M. Zhang, Y. Yang, Q. Huang, T. Fukuda, Z. Wang, and Y. Shen, "A Bioinspired Multilegged Soft Millirobot That Functions in Both Dry and Wet Conditions," *Nat. Commun.*, vol. 9, Sep. 2018, Art. no. 3944.

[9] W. Hu, G. Z. Lum, M. Mastrangeli, and M. Sitti, "Small-Scale Soft-Bodied Robot With Multimodal Locomotion," *Nature*, vol. 554, no. 7690, pp. 81–85, Feb. 2018.

[10] R. St. Pierre, W. Gosrich, and S. Bergbreiter, "A 3D-Printed 1 mg Legged Microrobot Running at 15 Body Lengths per Second," in *Proc. Solid-State Sens. Actuators Microsyst. Workshop*, Hilton Head Island, SC, USA, Jun. 2018, pp. 59–62.

[11] Y. Yang, X. Ye, and S. Guo, "A New Type of Jellyfish-Like Microrobot," in *Proc. IEEE Int. Conf. Integr. Technol.*, Shenzhen, China, Mar. 2007, pp. 59–62.

[12] M.-S. Kim, H.-T. Lee, and S.-H. Ahn, "Laser Controlled 65 Micrometer Long Microrobot Made of Ni-Ti Shape Memory Alloy," *Adv. Mater. Technol.*, vol. 4, no. 12, Dec. 2019, Art. no. 1900583.

[13] X.-T. Nguyen, A. A. Calderón, A. Rigo, J. Z. Ge, and N. O. Pérez-Arancibia, "SMALLBug: A 30-mg Crawling Robot Driven by a High-Frequency Flexible SMA Microactuator," *IEEE Robot. Automat. Lett.*, vol. 5, no. 4, pp. 6796–6803, Oct. 2020.

[14] R. M. Bena, X.-T. Nguyen, A. A. Calderón, A. Rigo, and N. O. Pérez-Arancibia, "SMARTI: A 60-mg Steerable Robot Driven by High-Frequency Shape-Memory Alloy Actuation," *IEEE Robot. Automat. Lett.*, vol. 6, no. 4, pp. 8173–8180, Oct. 2020.

[15] X. Yang, L. Chang, and N. O. Pérez-Arancibia, "An 88-Milligram Insect-Scale Autonomous Crawling Robot Driven by a Catalytic Artificial Muscle," *Sci. Robot.*, vol. 5, no. 45, Aug. 2020, Art. no. eaba0015.

[16] D. C. Lagoudas, *Shape Memory Alloys: Modeling and Engineering Applications*. New York, NY, USA: Springer, 2008.

[17] J. Z. Ge, L. Chang, and N. O. Pérez-Arancibia, "Position Control of a Shape-Memory Alloy Actuator Using a Preisach-Model-Based Inverse-Temperature Method," in *Proc. Amer. Control Conf. (ACC)*, Philadelphia, PA, USA, Jul. 2019, pp. 3801–3808.

[18] B. Chang, Q. Zhou, Z. Wu, Z. Liu, R. H. A. Ras, and K. Hjort, "Capillary Self-Alignment of Microchips on Soft Substrates," *Micromachines*, vol. 7, no. 3, Mar. 2016, Art. no. 41.

[19] M. Mastrangeli, Q. Zhou, V. Sariola, and P. Lambert, "Surface Tension-Driven Self-Alignment," *Soft Matter*, vol. 13, no. 2, pp. 304–327, Jan. 2017.

[20] X. Yang, Y. Chen, L. Chang, A. A. Calderón, and N. O. Pérez-Arancibia, "Bee$^+$: A 95-mg Four-Winged Insect-Scale Flying Robot Driven by Twinned Unimorph Actuators," *IEEE Robot. Automat. Lett.*, vol. 4, no. 4, pp. 4270–4277, Oct. 2019.

[21] D. L. Hu, B. Chan, and J. W. M. Bush, "The Hydrodynamics of Water Strider Locomotion," *Nature*, vol. 424, no. 6949, pp. 663–666, Aug. 2003.

[22] X. Gao and L. Jiang, "Water-Repellent Legs of Water Striders," *Nature*, vol. 432, no. 7013, p. 36, Nov. 2004.

[23] J. H. Yan, X. B. Zhang, J. Zhao, G. F. Liu, H. G. Cai, and Q. M. Pan, "A Miniature Surface Tension-Driven Robot Using Spatially Elliptical Moving Legs to Mimic a Water Strider's Locomotion," *Bioinspir. Biomim.*, vol. 10, no. 4, Aug. 2015, Art. no. 046016.

[24] J.-S. Koh, E. Yang, G.-P. Jung, S.-P. Jung, J. H. Son, S.-I. Lee, P. G. Jablonski, R. J. Wood, H.-Y. Kim, and K.-J. Cho, "Jumping on Water: Surface Tension–Dominated Jumping of Water Striders and Robotic Insects," *Science*, vol. 349, no. 6247, pp. 517–521, Jul. 2015.